AAAS
Research
Volume 2021, Article ID 9829374, 11 pages
https://doi.org/10.34133/2021/9829374

Research Article

Stable and Efficient Red Perovskite Light-Emitting Diodes Based on Ca^{2+}-Doped $CsPbI_3$ Nanocrystals

Wei Shen,[1] Jianbin Zhang,[1] Ruimin Dong,[1] Yanfeng Chen,[1] Liu Yang,[1] Shuo Chen,[1] Zhan Su,[1] Yujun Dai,[1] Kun Cao,[1] Lihui Liu,[1] Shufen Chen ,[1] and Wei Huang [2]

[1]*State Key Laboratory of Organic Electronics and Information Displays & Institute of Advanced Materials (IAM), Nanjing University of Posts & Telecommunications, 9 Wenyuan Road, Nanjing 210023, China*
[2]*Frontiers Science Center for Flexible Electronics (FSCFE), MIIT Key Laboratory of Flexible Electronics (KLoFE), Northwestern Polytechnical University, Xi'an 710072, China*

Correspondence should be addressed to Shufen Chen; iamsfchen@njupt.edu.cn and Wei Huang; iamwhuang@nwpu.edu.cn

Wei Shen and Jianbin Zhang contributed equally to this work.

Received 17 August 2021; Accepted 15 November 2021; Published 6 December 2021

α-$CsPbI_3$ nanocrystals (NCs) with poor stability prevent their wide applications in optoelectronic fields. Ca^{2+} (1.00 Å) as a new B-site doping ion can successfully boost $CsPbI_3$ NC performance with both improved phase stability and optoelectronic properties. With a Ca^{2+}/Pb^{2+} ratio of 0.40%, both phase and photoluminescence (PL) stability could be greatly enhanced. Facilitated by increased tolerance factor, the cubic phase of its solid film could be maintained after 58 days in ambient condition or 4 h accelerated aging process at 120°C. The PL stability of its solution could be preserved to 83% after 147 days in ambient condition. Even using UV light to accelerate aging, the T_{50} of PL could boost 1.8-folds as compared to $CsPbI_3$ NCs. Because Ca^{2+} doping can dramatically decrease defect densities of films and reduce hole injection barriers, the red light-emitting diodes (LEDs) exhibited about triple enhancement for maximum the external quantum efficiency (EQE) up to 7.8% and 2.2 times enhancement for half-lifetime of LED up to 85 min. We believe it is promising to further explore high-quality $CsPbI_3$ NC LEDs via a Ca^{2+}-doping strategy.

1. Introduction

All-inorganic perovskite ($CsPbX_3$, X = Cl, Br, I) nanocrystals (NCs) have the potential to promote the development of the luminescence and display industry due to their high photoluminescence quantum yields (PLQYs), high color purity, and solution processability [1–11]. Currently, green, red, and near-infrared perovskite light-emitting diodes (LEDs) have met the need of commercial demands from the efficiency factor (EQE > 20%) [2, 12], whereas $CsPbX_3$ NC-based LEDs are still underdeveloped. It should be noted that the high-performance optoelectronic properties of $CsPbX_3$ NCs are dominated by their crystal phase, especially for $CsPbI_3$ [13–17]. Generally, cubic (α) $CsPbI_3$ (direct band gap, E_g = 1.73 eV) exhibits good optoelectronic performance. However, the tolerance factor (τ) of α-$CsPbI_3$ is too small to stabilize its cubic phase at room temperature. The metastable state of α-$CsPbI_3$ can be easily transformed into the orthorhombic (δ) phase (E_g = 2.82 eV) with poor optoelectronic performance [3, 18–21]. Therefore, improving phase stability of α-$CsPbI_3$ is the foundation for achieving high-performance $CsPbI_3$ NC LEDs [22].

According to the Goldschmidt tolerance factor (τ) function for perovskite (ABX_3), doping ions with suitable size can realize precise tuning of τ to stabilize cubic phase [23, 24]. Based on this principle, A-, B-, or X-site doping can maintain α-$CsPbI_3$. It should be noted that common methods to synthesize $CsPbI_3$ NCs need high temperature (>170°C) [6]. As a result, organic A-site ions (methylamine or formamidine) will be easily decomposed at high temperature [24, 25]. Currently, B- or X-site doping is the hotspot for stabilization of α-$CsPbI_3$. Due to the ionic nature of

$CsPbI_3$, X-site ions are at the corner of the PbI_6^{4-} octahedron, which can easily migrate. With Br^- doping as an example, though $CsPbBr_xI_{3-x}$ NCs exhibit a cubic phase, the ion migration of Br^- and I^- easily leads to phase separation and degradation of optoelectronic performance [26], whereas B-site ions are at the center of the PbI_6^{4-} octahedron, which can hardly migrate. Therefore, B-site doping is the efficient way to stabilize α-$CsPbI_3$ without any side effects, such as thermal decomposition, or phase separation [27–30]. On the basis of the Goldschmidt tolerance factor function, doping with small-sized B-site ions can efficiently stabilize α-$CsPbI_3$ (Pb^{2+} radius 1.19 Å). For example, Mn^{2+} (0.67 Å) doping by direct synthesis or posttreatment methods can improve the stability of α-$CsPbI_3$ NCs from a few days to nearly a month under ambient conditions [31, 32]. In addition, B-site doping can not only enhance the stability of $CsPbI_3$ NCs but also boost their optoelectronic performance. Several B-site doping ions have been studied to promote the development of $CsPbI_3$ NC LEDs, such as Mn^{2+} [33], Zn^{2+} [34, 35], Zr^{2+} [36], Y^{3+} [35], Cu^{2+} [37], Ni^{2+} [38], and Sr^{2+} [39–41]. It should be emphasized that some doping ions, such as Zn^{2+}, Cu^{2+}, and Sr^{2+}, can reduce charge injection barriers and enhance carrier transport properties. To date, the state of the art for $CsPbI_3$ NC LEDs is facilitated by alkaline earth metal ion doping such as Sr^{2+} doping [39–41], which has the potential to satisfy the commercial demands [23]. It should be noted that the size of Sr^{2+} (1.18 Å) is almost the same as Pb^{2+} (1.19 Å). In other words, both stability and optoelectronic performance have more room to improve by doping other small size alkaline earth metal ions, such as Ca^{2+} (1.00 Å).

Herein, we explored Ca^{2+} as a new B-site doping ion to boost $CsPbI_3$ NC performance with both improved phase stability and optoelectronic properties. Doping Ca^{2+} to partly replace Pb^{2+} must increase τ. Therefore, Ca^{2+} doping can dramatically improve the phase stability of $CsPbI_3$ NCs, which suppresses the decreasing PLQY resulting from phase transition [33, 34, 40, 42]. Systematical studies on stability were done by tuning Ca^{2+}/Pb^{2+} ratios (0%, 0.35%, 0.40%, and 1.20%). For the case of 0.40% Ca^{2+}/Pb^{2+} ratios, Ca^{2+}-doped $CsPbI_3$ NCs showed enhanced phase stability to long-term storage and heat. Its solid film could exhibit the cubic phase after 58-day storage in ambient condition or 4 h accelerated aging process at 120°C. Additionally, its PL intensity in solution decayed less than 17% after 147-day storage in ambient condition. Even using UV light to accelerate aging, the half-lifetime of PL could boost 1.8-folds as compared to that of $CsPbI_3$ NCs. Furthermore, the Ca^{2+}-doped $CsPbI_3$ NCs were employed as the emission layer to fabricate LED. Benefitting from the Ca^{2+} doping, the defect densities were decreased to 21%, its valence band maximum went up to -5.55 eV to reduce hole injection barriers, and its lower Fermi level enhanced hole transport efficiency. As a result, Ca^{2+}-doped $CsPbI_3$ NC-based LED exhibited about triple enhancement for maximum EQE up to 7.8%, and 2.2 times enhancement for half-lifetime of LED up to 85 min. We believe it is promising to further explore high-quality $CsPbI_3$ NC LED via Ca^{2+}-doping strategy.

2. Result and Discussion

Ca^{2+}-doped $CsPbI_3$ NCs were synthesized by using different feed ratios of $Ca(Ac)_2/PbI_2$ (0%, 15%, 25%, and 35%) via hot injection method (Experimental Section). As shown in Table S1, the real Ca^{2+}/Pb^{2+} ratios for Ca^{2+}-doped $CsPbI_3$ NCs were determined by ICP-MS. According to ICP-MS results, the real Ca^{2+}/Pb^{2+} ratios were 0%, 0.35%, 0.40%, and 1.20% for the condition of 0%, 15%, 25%, and 35% feed ratios of $Ca(Ac)_2/PbI_2$. Such results implied that Ca^{2+} was successfully doped into $CsPbI_3$ NCs. The Pb^{2+} is located in the center of the octahedron (PbI_6^{4-}). The exchange and migration of the B-site ion is more difficult as compared to that of A-site and X-site ions. Therefore, B-site ions do not easily incorporate into the $CsPbI_3$ lattice, and the actual doping ratio of the B-site ion is much lower than the feed ratio [18, 34, 38, 40, 43]. The size of Ca^{2+} (1.00 Å) is smaller than Pb^{2+} (1.19 Å), and Ca^{2+} doping must induce the lattice contraction, which can be confirmed by XRD. Figure 1(a) shows XRD patterns for Ca^{2+}-doped $CsPbI_3$ NC films with different real Ca^{2+}/Pb^{2+} ratios. The patterns for all films match well with α-$CsPbI_3$ (PDF#97-018-1288), and the diffraction peaks at 14.09° and 28.58° correspond to the (100) and (200) planes, respectively [34]. It should be emphasized that the splitting peaks at around 14° may be related to γ-$CsPbI_3$ [44, 45], while the characterization patterns for γ-$CsPbI_3$ from 25-30° cannot be observed. It is possible that a slight lattice distortion occurred due to the influence of water and oxygen during the test [20, 46]. With increasing Ca^{2+}/Pb^{2+} ratio, no additional diffraction peaks were observed, which indicated that doping Ca^{2+} did not significantly change the $CsPbI_3$ crystal phase. Their fine XRD patterns are shown in Figure 1(b). There is a slight shift toward a higher diffraction angle for the α-$CsPbI_3$ (200) plane (28.62° for 0%, 28.77° for 0.35%, 28.78° for 0.40%, and 28.82° for 1.20%), which verifies the lattice contraction resulted from the partial replacement of Pb^{2+} (1.19 Å). An enhanced peak at 20° is attributed to the (110) crystal plane for $CsPbI_3$. Based on the HRTEM images, the cubic NCs become truncated cubic NCs (Figure S1a-d). Therefore, (110) crystal planes are more exposed and enhance the peak at 20° [47, 48]. Furthermore, the morphology and size characterization for Ca^{2+}-doped $CsPbI_3$ NCs were studied by TEM. As shown in Figures 1(c)–1(f), with increasing Ca^{2+}/Pb^{2+} ratio, Ca^{2+}-doped $CsPbI_3$ NCs maintain a cubic shape with uniform size distribution. The average size decreased from 11.11 ± 0.90 nm, 10.62 ± 0.98 nm, 10.40 ± 1.00 nm, and 9.89 ± 1.07 nm (Figure S2), which is mainly because Ca^{2+} doping influences lattice contraction or nucleation and growth processes. HRTEM images (Figures 1(g)–1(j)) reveal that Ca^{2+}-doped $CsPbI_3$ NCs are highly crystalline with displayed lattice fringes. The lattice distances of all samples are 0.31 nm corresponding to the (200) plane of α-$CsPbI_3$ [49]. This is due to the limited TEM accuracy, which makes it difficult to distinguish the difference of 0.001 nm. According to the XRD test results and Scherer's formula, the lattice distances of (200) are 0.311 nm (0%), 0.310 nm (0.8%), 0.310 nm (3.1%), and

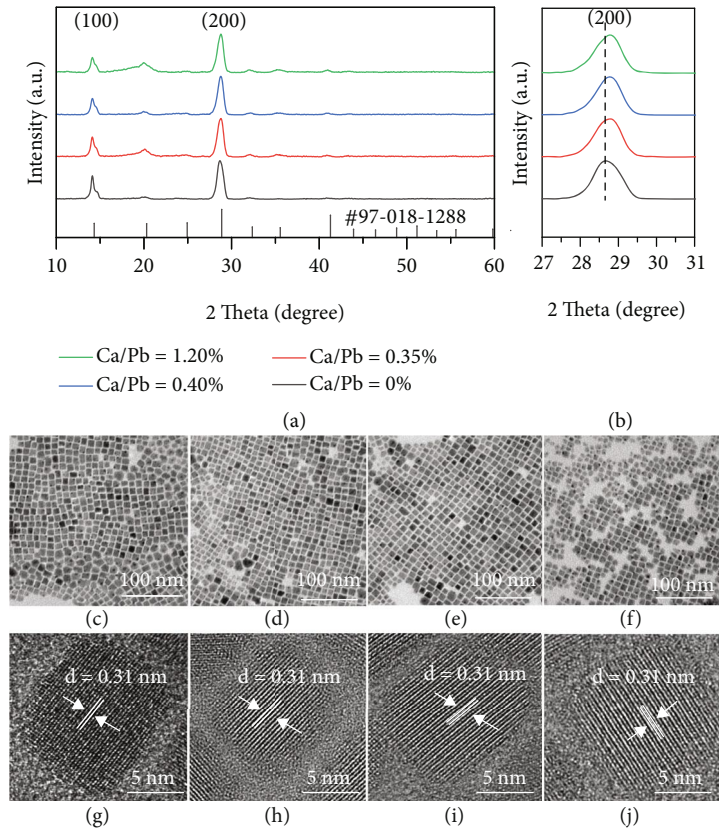

Figure 1: (a) XRD patterns of Ca^{2+}-doped $CsPbI_3$ NCs, (b) fine XRD patterns in the region of 27-31°, (c–f) TEM images of Ca^{2+}-doped $CsPbI_3$ NCs, (g–j) HRTEM images of Ca^{2+}-doped $CsPbI_3$ NCs (Ca/Pb = 0%, 0.35%, 0.40%, 1.20%).

0.309 nm (5.0%). Therefore, only XRD results can confirm that Ca^{2+} is successfully doped into $CsPbI_3$ NCs.

Furthermore, the elemental mapping images were measured by EDS (Figure S3a-d). We chose the elemental mapping area of Ca^{2+}-doped $CsPbI_3$ NCs in a high-angle annular dark field scanning transmission electron microscopy image (HAADF-STEM) (Figure 2(a)). Elemental mapping images of Cs, Pb, Ca, and I (Figures 2(b)–2(e)) can be observed clearly. We merged these elemental mapping images to obtain the overlapped image (Figure 2(f)), which shows that the positions of Cs, Pb, Ca, and I are uniformly distributed in NCs. Therefore, these results can directly demonstrate that Ca^{2+} is doped in $CsPbI_3$ NCs.

The optical properties of Ca^{2+}-doped $CsPbI_3$ NCs are shown in Figure 3. The UV-vis absorbance and PL spectra of Ca^{2+}-doped $CsPbI_3$ NCs are compared in Figure 3(a) and Figure S4a-b. With the ratio of Ca/Pb increasing, both of their UV-vis absorption and PL peaks appear as blue shifts due to their lattice contraction, size decrease, and Ca^{2+} orbitals to influence the electronic structure of NCs [34, 40, 50, 51] (Figure S4a-b and Figure S2). Figure 3(b) summarizes the UV-vis absorption peaks, PL peaks, and PLQY evolution with different ratios of Ca/Pb. The UV-vis absorption peaks exhibit a blue shift from 666 nm to 665, 664, and 661 nm with the ratio of Ca/Pb increasing from 0% to 0.35%, 0.40%, and 1.20%, respectively. Simultaneously, their PL peaks also exhibit a blue shift from 682 nm to 676 nm with increase of the ratio of Ca/Pb.

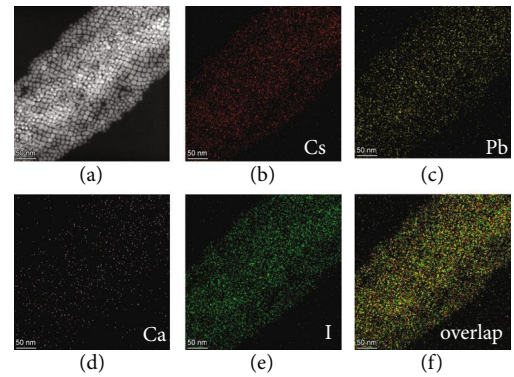

Figure 2: (a) HAADF-STEM images of Ca^{2+}-doped $CsPbI_3$ NCs and the corresponding elemental mapping images of Cs (b), Pb (c), Ca (d), I (e), and merged image (f). (b–f) Ca/Pb = 0.40%.

Furthermore, benefitting from Ca^{2+} doping, their PLQYs can be improved. With increasing Ca/Pb ratios from 0% to 0.40%, their PLQYs increased from 89% (±1.5%) to 93% (±1.3%), whereas further increasing the Ca/Pb ratio to 1.20% led PLQY lower to 91% (±1.4%). This is due to that the smaller NCs (Ca/Pb = 1.20%) with larger surface-to-volume ratio must have more surface defects. In addition, Ca^{2+} cannot be as emission centers. Therefore, excess Ca^{2+} doping may decrease PLQY. Figure 2(c) shows the decay curves of Ca^{2+}-doped $CsPbI_3$ NCs. All of the decay curves can be fitted by a double-exponential (Table S2). The

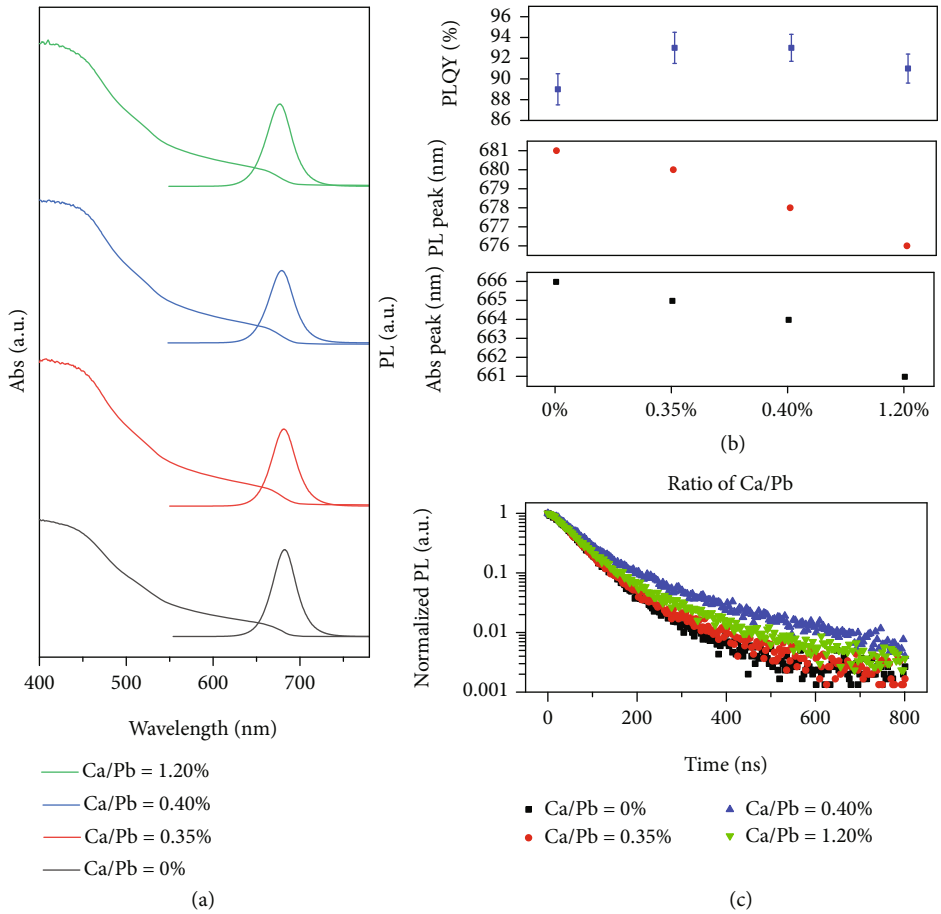

FIGURE 3: UV-vis absorption and PL spectra (a); UV-vis absorption peaks, PL peaks, and PLQYs (b); PL decay curves (c) of Ca^{2+}-doped $CsPbI_3$ NC solutions with different Ca/Pb ratios (Ca/Pb = 0%, 0.35%, 0.40%, 1.20%).

average PL lifetimes of Ca^{2+}-doped $CsPbI_3$ NCs are 71.76 ns (0%), 77.47 ns (0.35%), 119.47 ns (0.40%), and 92.62 ns (1.20%). Such results demonstrate that the improved τ facilitated by Ca^{2+} doping can reduce the lattice distortion and phase transition to maintain PLQYs at a relatively high level.

In addition to boosting their PLQYs, the increase in τ for Ca^{2+} doping in $CsPbI_3$ can much improve their stability. We measured the stability of their solutions and solid films. Firstly, all samples were stored in the conditions of $20 \pm 5°$ C and 40–50% humidity. Figure 4(a) shows PL intensity evolution with storage time. After a 147-day storage, PL intensity of $CsPbI_3$ NCs decreased to 36% of the initial one, whereas PL stabilities of Ca^{2+}-doped $CsPbI_3$ NCs exhibited much improvement. After 147-day storage, an obvious color bleaching was observed for the $CsPbI_3$ NC solution, while the red color of Ca^{2+}-doped $CsPbI_3$ NC solutions can be maintained (Figure 4(b)). PL intensities of Ca^{2+}-doped $CsPbI_3$ NC solutions can be preserved to 80% (0.35%), 83% (0.40%), and 76% (1.20%) of the initial intensities after 147-day storage (Figure 4(a) and Figure S5). We further studied their morphology changes by TEM. The size of $CsPbI_3$ NCs became nonuniform and noncubic shape and tended to be aggregated, which must lead to their PL decrease (Figure 4(c) and Figure S5). In contrast, cubic shape and uniform size distribution of Ca^{2+}-doped $CsPbI_3$ NCs can be kept with relatively high PL performance (Figure 4(c) and Figure S5). Secondly, Ca^{2+}-doped $CsPbI_3$ NCs exhibited improved stability against to UV. All of the samples were placed under 365 nm UV light (8 W), and their PL intensities decayed with UV irradiation time increasing. We periodically measured their PL spectra, which were used to calculate their half-lifetimes (T_{50}) under UV light (Figure S6 and Figure S7a). On the basis of these data, T_{50} were 52 min (0%), 74 min (0.35%), 92 min (0.40%), and 85 min (1.20%), separately. About 1.8 times enhancement of UV stability was observed for the 0.40% Ca/Pb ratio. Further increasing UV irradiation time to 100 min, it was hard to observe the red color for $CsPbI_3$ NCs, while Ca^{2+}-doped $CsPbI_3$ NCs could still emit red PL (Figure S7b). As a result, Ca^{2+}-doped $CsPbI_3$ NCs exhibit enhanced UV stability as compared to $CsPbI_3$ NCs.

According to the above results, Ca^{2+}-doped $CsPbI_3$ NC solutions exhibited improved stability in ambient condition and UV light, whereas the application of these NCs must form solid films. Therefore, we further studied their stability in solid films, such as in ambient condition (40–50% RH at $20 \pm 5°$C) and heating condition (120°C). As shown in Figure 5(a), α-$CsPbI_3$ (cubic phase) film gradually converted to δ-$CsPbI_3$ (orthorhombic phase) film after 28-day storage

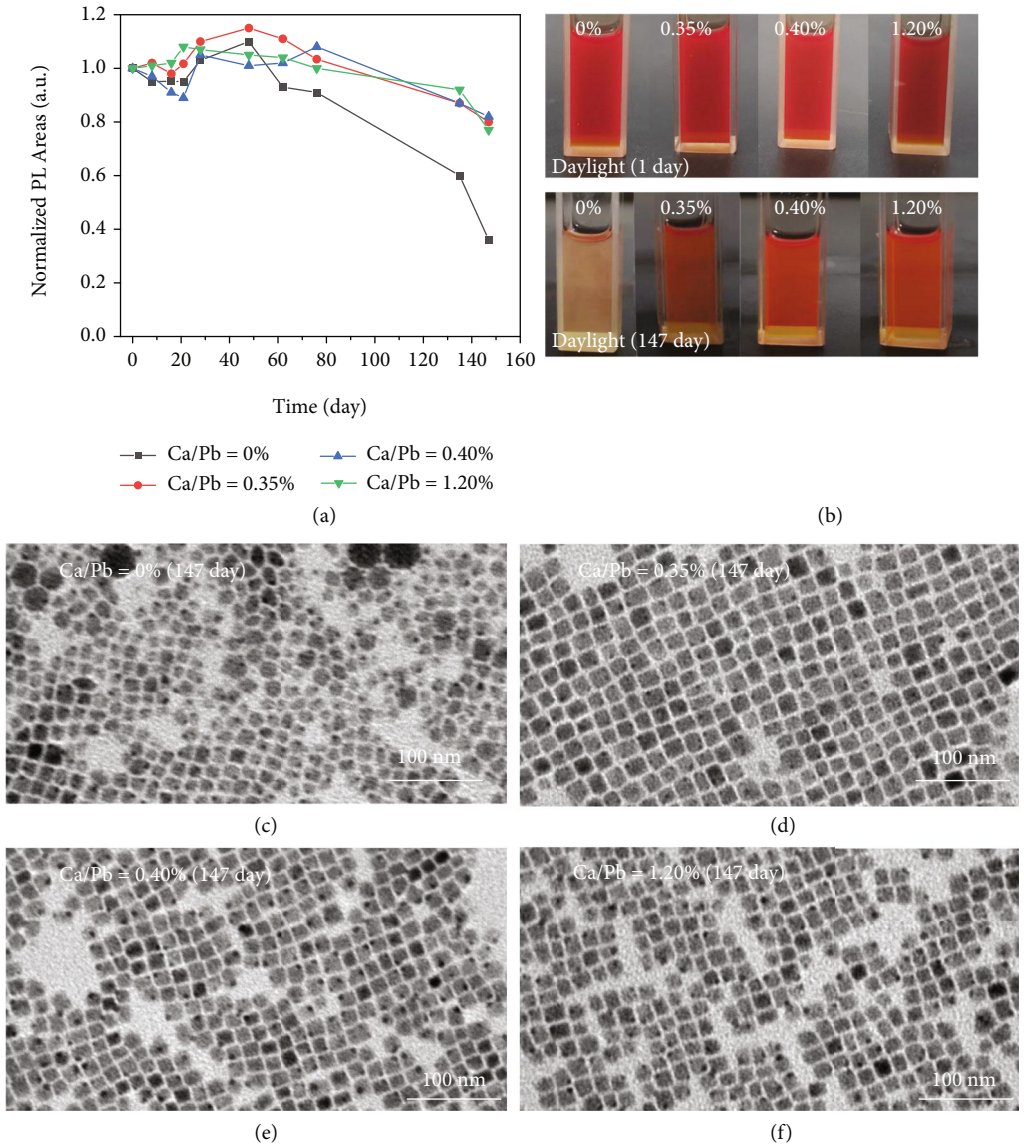

FIGURE 4: (a) The PL area evolution with increasing storing time in ambient condition; (b) images of the Ca^{2+}-doped $CsPbI_3$ NC solutions under daylight before and after 147-day storage (from left to right: Ca/Pb = 0%, 0.35%, 0.40%, 1.20%), and (c–f) TEM images of Ca^{2+}-doped $CsPbI_3$ NCs after 147-day storage.

time, and its color changed from red to yellow (Figure 5(e)). However, Ca^{2+}-doped $CsPbI_3$ films exhibited better crystal phase stability. The crystal phase of their films (Ca/Pb = 0.40%, 1.20%) could be maintained to the cubic phase after 58-day storage, which exhibited good PL performance (Figures 5(e) and 5(f)). Such results demonstrate that the phase stability of $CsPbI_3$ can be enhanced in ambient condition facilitated by Ca^{2+} doping. Additionally, we verified their thermal stability in the solid state. All the films were placed on a hot plate at 120°C, and we periodically measured their XRD patterns. The $CsPbI_3$ film exhibited the poorest phase stability, and its phase gradually converted to the orthorhombic phase after 120°C heating for 2 h (Figure S8). On the basis of previous reports, the small size effect can reduce $CsPbI_3$ lattice distortion to partly prevent phase transition [39, 52]. As an ionic nature of $CsPbI_3$, all ion migrations can be accelerated at high temperature. As a result, ion migration and crystal fusion easily occur in the solid state, which leads to increasing the size of $CsPbI_3$ NCs. The enlarged size of $CsPbI_3$ must induce phase transition [14, 53, 54]. Benefitting from small-sized Ca^{2+} doping, the increase in τ should improve the phase stability of $CsPbI_3$. With increase of the Ca/Pb ratio from 0% to 1.20%, their cubic phase could be maintained at least for 4 h at 120°C (Figure S8). Therefore, the thermal stability of $CsPbI_3$ films can be enhanced via Ca^{2+} doping.

To identify the positive effect of Ca^{2+}-doped $CsPbI_3$ NCs for LEDs, we used Ca^{2+}-doped $CsPbI_3$ NC films as emitting layers to fabricate red LEDs. Figure 6(a) is the energy-level diagram of LED. The LED architecture consists of a multiple-layered structure of ITO (170 nm)/PEDOT:PSS (30 nm)/Ca^{2+}-doped $CsPbI_3$ NCs (30 nm)/TPBi (40 nm)/LiF (1 nm)/Al (100 nm) shown in Figure S9. Herein, ITO is the anode; PEDOT:PSS is the hole-injection layer; TPBi

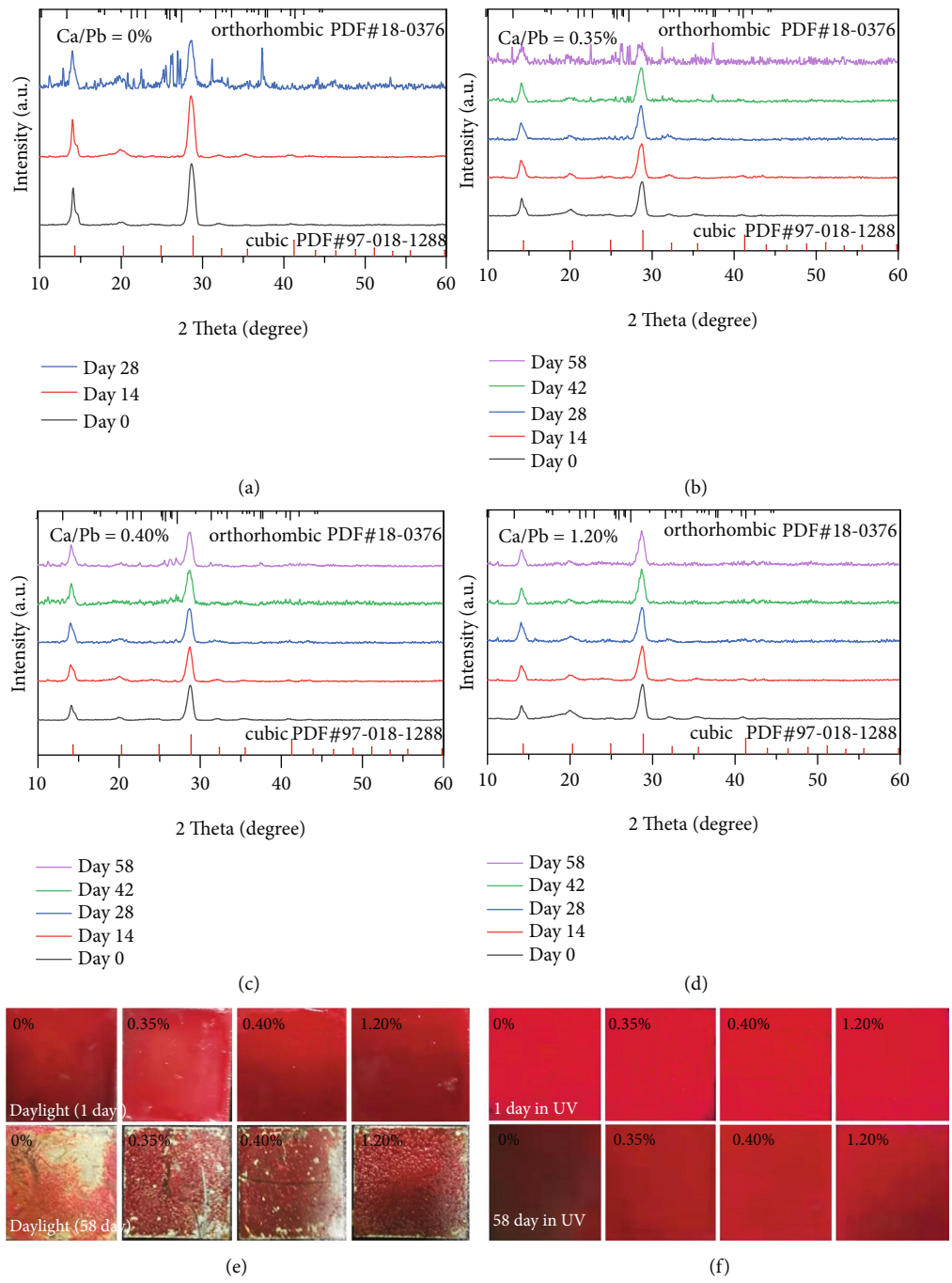

Figure 5: (a–d) XRD pattern evolution for Ca^{2+}-doped $CsPbI_3$ films in ambient condition (40–50% RH at 20 ± 5°C); images of Ca^{2+}-doped $CsPbI_3$ films under daylight (e) and under UV light (f) before and after 58-day storage in ambient condition.

and LiF are the electron-transport and electron-injection layer, respectively; and Al is the cathode. Figure 6(b) presents the current density as functions of voltage. The LED with Ca^{2+}-doped $CsPbI_3$ NCs (Ca/Pb = 0.40%) exhibited obviously enhanced current density, which implied the decreasing of defect density as well as the improvement for carrier transport efficiency.

Firstly, hole-only devices with a structure of ITO/PEDOT:PSS/$CsPbI_3$ NCs or Ca^{2+}-doped $CsPbI_3$ NCs/MoO_3/Al (Figure S10) were used to quantitatively measure the defect density of NCs films. The defect density (N_t) is calculated according to the following equation:

$$N_t = \frac{2\varepsilon\varepsilon_0 V_{\mathrm{TFL}}}{eL^2}, \tag{1}$$

where ε_0 and ε are the vacuum dielectric constant and the relative dielectric constant, respectively; V_{TFL} is the trap-filled limit voltage; L is the thickness of the NC film; and e is the elementary electronic charge. By assuming that ε =

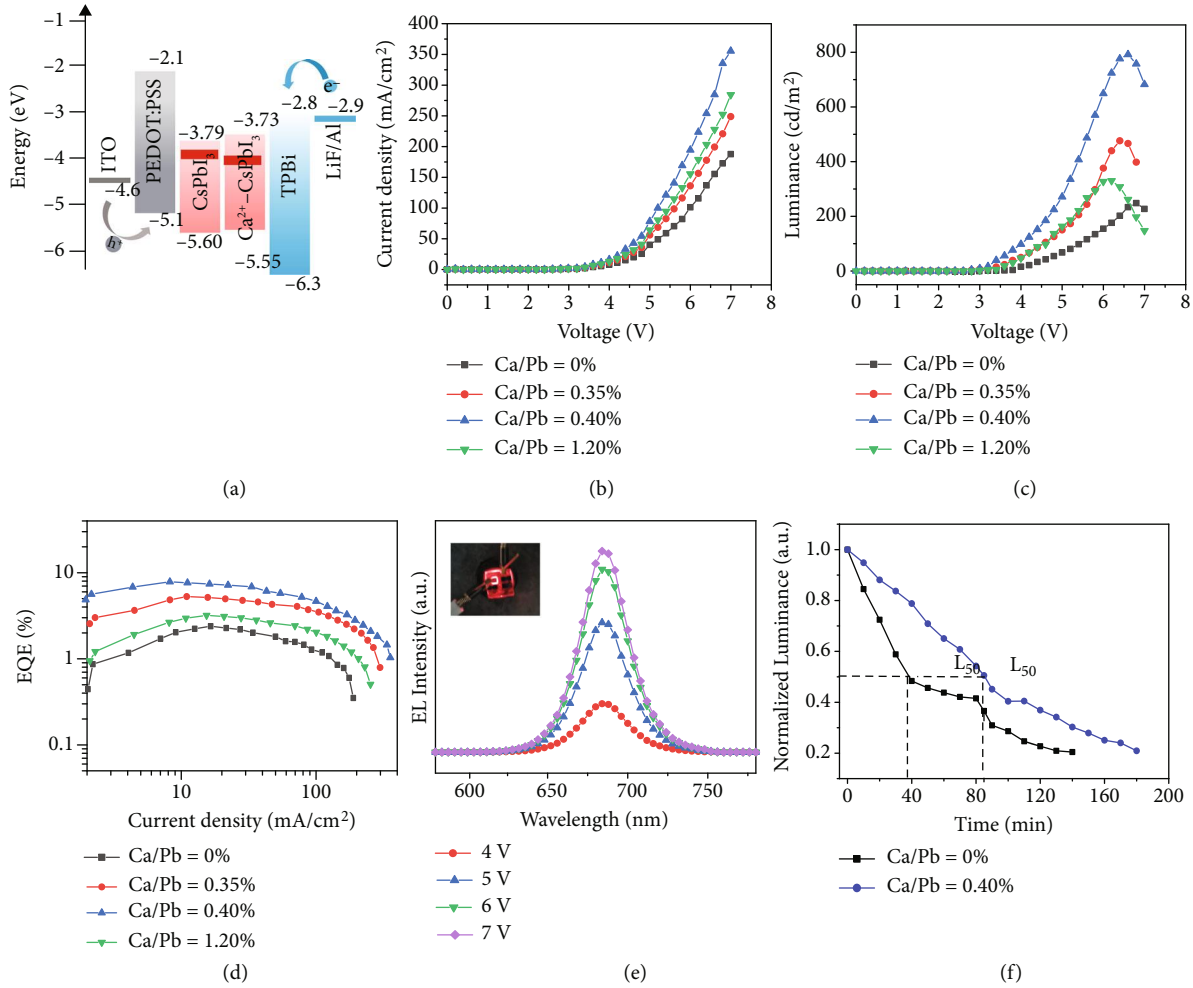

FIGURE 6: (a) LED energy-level diagram, (b) current density, (c) luminescence, and (d) EQEs for LEDs; (e) EL spectra of Ca^{2+}-doped $CsPbI_3$ NCs (0.40%) LEDs on various driving voltages and a photograph of the working device (inset in (e)); (f) operational stability of the LEDs at a constant current density of 5.0 mA/cm^2.

6.3 [34], the defect densities of $CsPbI_3$ and Ca^{2+}-doped $CsPbI_3$ NC films were 0.71×10^{17} and 0.15×10^{17} cm^{-3}, respectively. This means that the defect density could be decreased to 21.1% facilitated by 0.40% Ca^{2+} doping. Such results match with those results of PLQY and TRPL. In addition, the hole migration rates were estimated by fitting the space-charge-limited-current region (SCLC) with Child's law:

$$J = \frac{9\varepsilon\varepsilon_0\mu V^2}{8L^3}, \quad (2)$$

where ε_0 is the vacuum permittivity; ε_r is the average relative dielectric constant of $CsPbI_3$ ($\varepsilon_r \approx 6.32$); L is the thickness of the perovskite film; and J, μ, and V are the measured current density, carrier migration rates, and applied voltage, respectively [34]. The hole mobilities of $CsPbI_3$ and Ca^{2+}-doped $CsPbI_3$ NC films were 2.8×10^{-8} and 6.0×10^{-8} cm^{2}V^{-1} s^{-1}, respectively. With the Ca^{2+} doping, the hole mobility increased, which enhanced hole transport efficiency.

Then, the improvement for carrier transport efficiency can be confirmed by ultraviolet photoelectron spectra (UPS). Combining with their optical bandgaps (E_g) for Ca^{2+}-doped $CsPbI_3$ NC film (Figure S11a) and their UPS spectra of $CsPbI_3$ NCs (Figure S11b), their conduction band minimum (CBM), valence band maximum (VBM), and Fermi level can be obtained. For $CsPbI_3$ NCs, its CBM, VBM, and Fermi level were -3.79 eV, -5.60 eV, and -3.93 eV, respectively. Benefitting from Ca^{2+} doping (0.40%), its CBM, VBM, and Fermi level shifted to -3.73 eV, -5.55 eV, and -4.05 eV, respectively. The higher VBM reduces the energy barrier between PEDOT:PSS and the emission layer to boost hole transport efficiency. Additionally, the lower Fermi level reveals the transformation of $CsPbI_3$ NCs from n-type to a more nearly ambipolar nature facilitated by Ca^{2+} doping, which also enhances hole transport efficiency [34, 37].

Benefitting from the enhanced current density, the Ca^{2+}-doped $CsPbI_3$ NC LEDs exhibited stronger brightness than $CsPbI_3$ NC LEDs in the whole driving voltage range (Figure 6(c) and Figure S12). In the case of 0.40% Ca^{2+} doping, LED had a maximum luminance of 790 cd/m^2

(7.2 V), which was doubled as compared to the nondoping one. In addition, the maximum and average EQEs for Ca^{2+}-doped $CsPbI_3$ NC (0.40%) LEDs were 7.8% and 6.3%, both of which enhanced to about 3 times as compared to the nondoping one, respectively (Figure 6(d) and Figure S13). Therefore, our work using Ca^{2+} as a new B-site doping ion to boost $CsPbI_3$ NC LEDs is quite promising (Table S3). Their electroluminescent (EL) spectra exhibit stable and sharp peaks at 683 nm with a full width at half-maximum (FWHM) of 35 nm on various driving voltages (Figure 6(e) and Figure S14). A bright red emission could be observed at 5.0 V (inset in Figure 6(e)), and its Commission Internationale del'Eclairage (CIE) color coordinate was (0.72, 0.27) (Figure S15). Furthermore, the operational stability of the LED was evaluated at a constant current density of 5.0 mA/cm^2. The luminance of $CsPbI_3$ NC LEDs decreases to half at 39 min, while the half-lifetime of Ca^{2+}-doped $CsPbI_3$ NC (0.40%) LEDs could significantly increase to 85 min. A 2.2-fold improvement for the half-lifetime of LED confirmed that Ca^{2+} doping is a powerful strategy to promote both stability of $CsPbI_3$ NCs and their LEDs. In a word, the boosting of both the efficiency and the stability of LEDs is mainly attributed to a decrease in defect density, improvement on hole injection efficiency, and reduction in phase transition.

3. Conclusion

In summary, we explored stable and high-performance $CsPbI_3$ NCs based on Ca^{2+} (1.00 Å) doping. With a Ca^{2+}/Pb^{2+} ratio of 0.40%, the phase stability could be greatly enhanced. Ca^{2+}-doped $CsPbI_3$ NC solid films could maintain the cubic phase after 58-day storage in ambient condition or 4 h accelerated aging process at 120°C. Moreover, the PL stability could be also improved. The PL intensity of Ca^{2+}-doped $CsPbI_3$ NC solutions could be preserved to 83% after 147-day storage in ambient condition. Even using UV light to accelerate aging, the T_{50} of PL could be boosted 1.8-folds as compared to that of $CsPbI_3$ NCs. Red LED based on Ca^{2+}-doped $CsPbI_3$ NCs exhibited about triple enhancement for maximum EQE up to 7.8% and 2.2 times enhancement for half-lifetime of LED up to 85 min. These were mainly attributed to the decreased defect densities of films and reduced hole injection barrier facilitated by Ca^{2+} doping. Ca^{2+} as a new B-site doping ion can efficiently boost both stability and performance for $CsPbI_3$ NC LEDs, which has the potential to promote the development of $CsPbI_3$ NC LEDs.

4. Experimental Section

4.1. Chemical Materials. Oleic acid (OA, 90%), 1-octadecene (ODE, 90%), methyl acetate (MeOAc, 99%), hydriodic acid (HI, 57%) oleylamine (OLA, 80-90%), cesium carbonate (Cs_2CO_3, 99.99%), calcium acetate ($Ca(Ac)_2$, 95%), and lead iodide (PbI_2, 99.99%) were purchased from Aladdin. Poly(3,4-ethylenedioxythiophene):poly(4-styrenesulphonate) (PEDOT:PSS, CLEVIOS P VP AI 4083) was purchased from Heraeus Materials Technology Co. Ltd. 2,2′,2″-(1,3,5-Benzinetriyl)-tris(1-phenyl-1-H-benzimidazole) (TPBi) was purchased from Nichem Fine Technology Co. Ltd. All the chemicals were directly used without further purification.

4.2. Synthesis of Cs-OA. 0.39 g Cs_2CO_3, 18 mL ODE, and 2.0 mL OA were mixed into a 100 mL three-neck flask and dried in vacuum at 120°C for 1 h. Then, the mixture was heated to 150°C under N_2 until the Cs_2CO_3 powders were completely dissolved to form a transparent solution. The solution was cooled down to room temperature via ice-water bath and preheated to 110°C before use.

4.3. Synthesis of OLA-HI. 20 mL OLA and 2 mL HI were mixed into a 100 mL three-neck flask. Then, the solution was heated to 120°C for 2 h under vacuum to remove the water. Then, the solution was cooled down to 60°C to obtain the OLA-HI solution and preheated to 90°C before use.

4.4. Synthesis of Ca^{2+}-Doped $CsPbI_3$ NCs. In a typical synthesis, PbI_2 (0.4 mmol), $Ca(Ac)_2$ (0, 0.06, 0.10, and 0.14 mmol), and 10 mL ODE were mixed into a 100 mL three-neck flask. The mixture was degassed and dried in vacuum for 1 h at 120°C. Then, 1.0 mL OLA, OA, and preheated OLA-HI were injected into the reaction flask, separately. The mixed solution became clear and was kept under vacuum for 30 min at 120°C. Finally, the temperature was increased to 260°C, and 1.0 mL Cs-OA solution was injected immediately. After 1 min, the reaction flask was placed into an ice-water bath to stop the reaction.

4.5. Purification of NCs. The as-prepared NC solution was mixed with the same volume of MeOAc and was centrifuged at 15000 rpm for 5 min at 19°C to remove the supernatant. The precipitate was redispersed into toluene. Then, the NC toluene solution was mixed with the same volume of MeOAc and was centrifuged at 15000 rpm for 5 min at 19°C. After removing the supernatant, the precipitate was dispersed into toluene. Finally, the redispersed NC solution was centrifuged at 15000 rpm for 5 min at 19°C to discard the precipitate, and the supernatant was preserved for characterization and device fabrication.

4.6. Fabrication of LED Devices. Indium tin oxide- (ITO-) coated glass substrates were cleaned by ultrasonic cleaning for 15 min in acetone, ethanol, and deionized water, separately, and dried with nitrogen flow. The clean ITO glasses were treated by UV-ozone for 15 min. Then, PEDOT:PSS solutions were spin-coated onto the ITO substrates at 3000 rpm for 30 s and annealed at 120°C for 15 min in air. NCs were spin-coated onto the PEDOT:PSS layer at 1500 rpm for 30 s. This process was repeated five times. Finally, 40 nm of the TPBi layer, 1 nm of the LiF layer, and 100 nm of Al electrode were deposited in sequence by a thermal evaporation system under a high vacuum (~2×10^{-4} Pa). The active area of the devices was 10 mm^2 as defined by the overlapping area of the ITO and Al electrodes.

4.7. Characterizations. The ultraviolet-visible (UV-Vis) absorption spectra of NC solutions were measured by a PerkinElmer Lambda 35S instrument in transmission mode. PL

spectra were collected by a RF6000 spectrofluorometer with an excitation wavelength of 500 nm. The PL lifetimes of NCs were measured by a FLS920 fluorescence spectrometer with a pulse laser at 375 nm. The chemical compositions were measured by a PerkinElmer NexION 2000 inductively coupled plasma mass spectrometry (ICP-MS). X-ray diffraction (XRD) data were collected by a Bruker D8 Advance X-ray powder diffractometer with Cu Kα radiation ($\lambda = 0.154$ nm). Photoluminescence fluorescence quantum yield (PLQY), which is defined as the ratio of emitted photons to absorbed ones, was determined by a FLS920 fluorescence spectrometer equipped with an integrating sphere. The morphology and size of NCs were confirmed by transmission electron microscope (TEM) (Hitachi, HT7700), high-resolution TEM (HRTEM) (Talos, F200X), and energy-dispersive X-ray spectroscopy (EDS). The electroluminescent (EL) spectra and luminance- (L-) current density- (J-) voltage (V) characteristics were collected by using a Keithley 2400 source and PR-655 spectra scan spectrophotometer (Photo Research). The characterization for LED devices was measured at room temperature in air.

Data Availability

All data needed to evaluate the conclusions in the paper are presented in the paper and/or the Supplementary Materials. Additional data related to this paper may be requested from the authors.

Conflicts of Interest

The authors declare no conflict of interest.

Authors' Contributions

W. Shen and J. Zhang contributed equally to this work and are listed as co-first authors. S. Chen and W. Huang conceived and designed the research and revised the manuscript. W. Shen and J. Zhang performed the synthesis, data analysis, and article writing. R. Dong, Y. Chen, and S. Chen prepared and characterized the LED. L. Yang, Z. Su, and Y. Dai acquired the stability data. L. Liu and K. Cao assisted in all data analysis and interpretation. All authors participated in drafting the manuscript and approved the final version.

Acknowledgments

This work was supported by the National Major Fundamental Research Program of China (Grant No. 91833306), the National Natural Science Foundation of China (Grant Nos. 62074083, 62005131, and 61705111), the Natural Science Foundation of Jiangsu Province (Grant No. BM2012010), the Natural Science Fund for Colleges and Universities in Jiangsu Province (Grant No. 20KJA510005), the Priority Academic Program Development of Jiangsu Higher Education Institutions (Grant No. YX030003), NUPTSF (Grant Nos. NY219158 and NY220025), and the Postgraduate Research & Practice Innovation Program of Jiangsu Province (KYCX20_0754).

Supplementary Materials

Supplementary 1. Figure S1: HRTEM images of Ca^{2+}-doped $CsPbI_3$ NCs. Figure S2: statistical histogram particle size. Figure S3: EDX spectrum of Ca^{2+}-doped $CsPbI_3$ NCs. Figure S4: normalized UV-vis absorption and normalized PL spectra. Figure S5: the PL evolution of Ca^{2+}-doped $CsPbI_3$ NC solutions with increase of storing time. Figure S6: the PL area evolution with increasing irradiation time. Figure S7: the PL evolution of Ca^{2+}-doped $CsPbI_3$ NCs under 365 nm. Figure S8: XRD patterns evolution for Ca^{2+}-doped $CsPbI_3$ NC thin films at 120°C. Figure S9. the cross-section SEM image of LEDs. Figure S10: J-V curves of "hole-only" devices. Figure S11: E_g and UPS of Ca^{2+}-doped CsPbI3 NCs. Figure S12: current density and luminescence for LEDs. Figure S13: histogram of EQEs for 10 LEDs. Figure S14: (a–d) normalized EL spectra of Ca^{2+}-doped $CsPbI_3$ NCs. Figure S15: the corresponding CIE coordinates for the EL spectra. Table S1: ICP-MS data. Table S2: the time-resolved PL decays. Table S3: current $CsPbI_3$ NC LED performance with similar structure. *(Supplementary Materials)*

References

[1] A. Dutta, R. K. Behera, P. Pal, S. Baitalik, and N. Pradhan, "Near-unity photoluminescence quantum efficiency for all $CsPbX_3$(X=Cl, Br, and I) perovskite nanocrystals: a generic synthesis approach," *Angewandte Chemie International Edition*, vol. 58, no. 17, pp. 5552–5556, 2019.

[2] X. K. Liu, W. Xu, S. Bai et al., "Metal halide perovskites for light-emitting diodes," *Nature Materials*, vol. 20, no. 1, pp. 10–21, 2021.

[3] H. Huang, M. I. Bodnarchuk, S. V. Kershaw, M. V. Kovalenko, and A. L. Rogach, "Lead halide perovskite nanocrystals in the research spotlight: stability and defect tolerance," *ACS Energy Letters*, vol. 2, no. 9, pp. 2071–2083, 2017.

[4] Y. Wu, C. Wei, X. Li et al., "In situ passivation of PbBr64–Octahedra toward blue luminescent CsPbBr3Nanoplatelets with near 100% absolute quantum yield," *ACS Energy Letters*, vol. 3, no. 9, pp. 2030–2037, 2018.

[5] F. Liu, Y. Zhang, C. Ding et al., "Highly luminescent phase-stable CsPbI3Perovskite quantum dots achieving near 100% absolute photoluminescence quantum yield," *ACS Nano*, vol. 11, no. 10, pp. 10373–10383, 2017.

[6] J. Shamsi, A. S. Urban, M. Imran, L. de Trizio, and L. Manna, "Metal halide perovskite nanocrystals: synthesis, post-synthesis modifications, and their optical properties," *Chemical Reviews*, vol. 119, no. 5, pp. 3296–3348, 2019.

[7] N. Pradhan, "Tips and twists in making high photoluminescence quantum yield perovskite nanocrystals," *ACS Energy Letters*, vol. 4, no. 7, pp. 1634–1638, 2019.

[8] L. Liu, R. Dong, D. Ye et al., "Phosphomolybdic acid-modified monolayer graphene anode for efficient organic and perovskite light-emitting diodes," *ACS Applied Materials & Interfaces*, vol. 13, no. 10, pp. 12268–12277, 2021.

[9] W. Shen, Y. Lu, P. Xia et al., "A donor–acceptor ligand boosting the performance of $FA_{0.8}Cs_{0.2}PbBr_3$ nanocrystal light-emitting diodes," *Nanoscale*, vol. 13, no. 3, pp. 1791–1799, 2021.

[10] P. Xia, Y. Lu, Y. Li et al., "Solution-processed quasi-two-dimensional/nanoscrystals perovskite composite film enhances the

efficiency and stability of perovskite light-emitting diodes," *ACS Applied Materials & Interfaces*, vol. 12, no. 35, pp. 39720–39729, 2020.

[11] Y.-H. Kim, S. Kim, A. Kakekhani et al., "Comprehensive defect suppression in perovskite nanocrystals for high- efficiency light-emitting diodes," *Nature Photonics*, vol. 15, no. 2, pp. 148–155, 2021.

[12] Y. K. Wang, F. Yuan, Y. Dong et al., "All-inorganic quantum-dot LEDs based on a phase-stabilized α-CsPbI3Perovskite," *Angewandte Chemie International Edition*, vol. 60, no. 29, pp. 16164–16170, 2021.

[13] Y. Wang, Y. Chen, T. Zhang, X. Wang, and Y. Zhao, "Chemically stable black phase $CsPbI_3$ Inorganic perovskites for high-efficiency photovoltaics," *Advanced Materials*, vol. 32, no. 45, article 2001025, 2020.

[14] J. C. Yu, D. W. Kim, D. B. Kim et al., "Improving the stability and performance of perovskite light-emitting diodes by thermal annealing treatment," *Advanced Materials*, vol. 28, no. 32, pp. 6906–6913, 2016.

[15] J. Shi, F. Li, Y. Jin et al., "In situ ligand bonding management of CsPbI3Perovskite quantum dots enables high-performance photovoltaics and red light-emitting diodes," *Angewandte Chemie International Edition*, vol. 59, no. 49, pp. 22230–22237, 2020.

[16] Y. Tang, A. Lesage, and P. Schall, "CsPbI3nanocrystal films: towards higher stability and efficiency," *Journal of Materials Chemistry C*, vol. 8, no. 48, pp. 17139–17156, 2020.

[17] Z. du, D. Fu, J. Teng et al., "$CsPbI_3$ Nanotube photodetectors with high detectivity," *Small*, vol. 15, no. 52, article 1905253, 2019.

[18] A. Swarnkar, W. J. Mir, and A. Nag, "Can B-site doping or alloying improve thermal- and phase-stability of all-inorganic $CsPbX_3$ (X = Cl, Br, I) perovskites?," *ACS Energy Letters*, vol. 3, no. 2, pp. 286–289, 2018.

[19] A. Marronnier, G. Roma, S. Boyer-Richard et al., "Anharmonicity and disorder in the black phases of cesium lead iodide used for stable inorganic perovskite solar cells," *ACS Nano*, vol. 12, no. 4, pp. 3477–3486, 2018.

[20] B. Wang, N. Novendra, and A. Navrotsky, "Energetics, structures, and phase transitions of cubic and orthorhombic cesium lead iodide ($CsPbI_3$) polymorphs," *Journal of the American Chemical Society*, vol. 141, no. 37, pp. 14501–14504, 2019.

[21] S. Masi, A. F. Gualdrón-Reyes, and I. Mora-Seró, "Stabilization of black perovskite phase in FAPbI3and $CsPbI_3$," *ACS Energy Letters*, vol. 5, no. 6, pp. 1974–1985, 2020.

[22] H. Li, H. Lin, D. Ouyang et al., "Efficient and stable red perovskite light-emitting diodes with operational stability >300 h," *Advanced Materials*, vol. 33, no. 15, article 2008820, 2021.

[23] L. Xu, S. Yuan, H. Zeng, and J. Song, "A comprehensive review of doping in perovskite nanocrystals/quantum dots: evolution of structure, electronics, optics, and light-emitting diodes," *Materials Today Nano*, vol. 6, article 100036, 2019.

[24] C. H. Lu, G. V. Biesold-McGee, Y. Liu, Z. Kang, and Z. Lin, "Doping and ion substitution in colloidal metal halide perovskite nanocrystals," *Chemical Society Reviews*, vol. 49, no. 14, pp. 4953–5007, 2020.

[25] J. A. Vigil, A. Hazarika, J. M. Luther, and M. F. Toney, "$FA_xCs_{1-x}PbI_3$ Nanocrystals: tuning crystal symmetry by A-site cation composition," *ACS Energy Letters*, vol. 5, no. 8, pp. 2475–2482, 2020.

[26] A. F. Gualdrón-Reyes, S. J. Yoon, E. M. Barea et al., "Controlling the phase segregation in mixed halide perovskites through nanocrystal size," *ACS Energy Letters*, vol. 4, no. 1, pp. 54–62, 2019.

[27] Y. Zou, Z. Yuan, S. Bai, F. Gao, and B. Sun, "Recent progress toward perovskite light-emitting diodes with enhanced spectral and operational stability," *Materials Today Nano*, vol. 5, article 100028, 2019.

[28] S. Bera, D. Ghosh, A. Dutta, S. Bhattacharyya, S. Chakraborty, and N. Pradhan, "Limiting heterovalent B-site doping in CsPbI3Nanocrystals: phase and optical stability," *ACS Energy Letters*, vol. 4, no. 6, pp. 1364–1369, 2019.

[29] M. I. Ustinova, M. M. Mikheeva, G. V. Shilov et al., "Partial substitution of Pb^{2+} in $CsPbI_3$ as an efficient strategy to design fairly stable all-inorganic perovskite formulations," *ACS Applied Materials & Interfaces*, vol. 13, no. 4, pp. 5184–5194, 2021.

[30] Y. Ji, J. B. Zhang, H. R. Shen et al., "Improving the stability of α-$CsPbI_3$ Nanocrystals in extreme conditions facilitated by Mn^{2+} Doping," *ACS Omega*, vol. 6, no. 21, pp. 13831–13838, 2021.

[31] Q. A. Akkerman, D. Meggiolaro, Z. Dang, F. de Angelis, and L. Manna, "Fluorescent alloy CsPbxMn1–xI3Perovskite nanocrystals with high structural and optical stability," *ACS Energy Letters*, vol. 2, no. 9, pp. 2183–2186, 2017.

[32] W. J. Mir, A. Swarnkar, and A. Nag, "Postsynthesis Mn-doping in CsPbI3nanocrystals to stabilize the black perovskite phase," *Nanoscale*, vol. 11, no. 10, pp. 4278–4286, 2019.

[33] S. Zou, Y. Liu, J. Li et al., "Stabilizing cesium lead halide perovskite lattice through Mn(II) substitution for air-stable light-emitting diodes," *Journal of the American Chemical Society*, vol. 139, no. 33, pp. 11443–11450, 2017.

[34] X. Shen, Y. Zhang, S. V. Kershaw et al., "Zn-alloyed $CsPbI_3$ Nanocrystals for highly efficient perovskite light-emitting devices," *Nano Letters*, vol. 19, no. 3, pp. 1552–1559, 2019.

[35] J. Li, J. Chen, L. Xu et al., "A zinc non-halide dopant strategy enables efficient perovskite $CsPbI_3$ quantum dot-based light-emitting diodes," *Materials Chemistry Frontiers*, vol. 4, no. 5, pp. 1444–1453, 2020.

[36] M. Lu, J. Guo, S. Sun et al., "A zinc non-halide dopant strategy enables efficient perovskite $CsPbI_3$ quantum dot-based light-emitting diodes," *Nano Letters*, vol. 20, no. 4, pp. 2829–2836, 2020.

[37] Z. Chen, B. Zhou, J. Yuan et al., "Cu^{2+}-Doped $CsPbI_3$ Nanocrystals with enhanced stability for light-emitting diodes," *The Journal of Physical Chemistry Letters*, vol. 12, no. 12, pp. 3038–3045, 2021.

[38] M. Liu, N. Jiang, H. Huang et al., "Ni^{2+}-doped $CsPbI_3$ perovskite nanocrystals with near-unity photoluminescence quantum yield and superior structure stability for red light-emitting devices," *Chemical Engineering Journal*, vol. 413, article 127547, 2021.

[39] M. Lu, X. Zhang, Y. Zhang et al., "Simultaneous strontium doping and chlorine surface passivation improve luminescence intensity and stability of $CsPbI_3$ Nanocrystals enabling efficient light-emitting devices," *Advanced Materials*, vol. 30, no. 50, article 1804691, 2018.

[40] J. S. Yao, J. Ge, K. H. Wang et al., "Few-nanometer-sized α-CsPbI3Quantum dots enabled by strontium substitution and iodide passivation for efficient red-light emitting diodes," *Journal of the American Chemical Society*, vol. 141, no. 5, pp. 2069–2079, 2019.

[41] C. Chen, T. Xuan, W. Bai et al., "Highly stable $CsPbI_3$:Sr^{2+} nanocrystals with near-unity quantum yield enabling perovskite light-emitting diodes with an external quantum efficiency of 17.1%," *Nano Energy*, vol. 85, article 106033, 2021.

[42] W. Liu, Q. Lin, H. Li et al., "Mn^{2+}-Doped lead halide perovskite nanocrystals with dual-color emission controlled by halide content," *Journal of the American Chemical Society*, vol. 138, no. 45, pp. 14954–14961, 2016.

[43] C. Eames, J. M. Frost, P. R. F. Barnes, B. C. O'Regan, A. Walsh, and M. S. Islam, "Ionic transport in hybrid lead iodide perovskite solar cells," *Nature Communications*, vol. 6, no. 1, p. 7497, 2015.

[44] Q. Zhao, A. Hazarika, L. T. Schelhas et al., "Size-dependent lattice structure and confinement properties in CsPbI3Perovskite nanocrystals: negative surface energy for stabilization," *ACS Energy Letters*, vol. 5, no. 1, pp. 238–247, 2020.

[45] R. J. Sutton, M. R. Filip, A. A. Haghighirad et al., "Cubic or orthorhombic? Revealing the crystal structure of metastable black-phase CsPbI3by theory and experiment," *ACS Energy Letters*, vol. 3, no. 8, pp. 1787–1794, 2018.

[46] J.-K. Sun, S. Huang, X.-Z. Liu et al., "Polar solvent induced lattice distortion of cubic CsPbI3Nanocubes and hierarchical self-assembly into orthorhombic single-crystalline nanowires," *Journal of the American Chemical Society*, vol. 140, no. 37, pp. 11705–11715, 2018.

[47] S. Narayanan, G. Cheng, Z. Zeng, Y. Zhu, and T. Zhu, "Strain hardening and size effect in five-fold twinned ag nanowires," *Nano Letters*, vol. 15, no. 6, pp. 4037–4044, 2015.

[48] Y. Liu, Y. Dong, T. Zhu et al., "Bright and stable light-emitting diodes based on perovskite quantum dots in perovskite matrix," *Journal of the American Chemical Society*, vol. 143, no. 38, pp. 15606–15615, 2021.

[49] J. Pan, Y. Shang, J. Yin et al., "Bidentate ligand-passivated CsPbI3Perovskite nanocrystals for stable near-unity photoluminescence quantum yield and efficient red light-emitting diodes," *Journal of the American Chemical Society*, vol. 140, no. 2, pp. 562–565, 2018.

[50] C. Lu, J. Zhang, D. Hou et al., "Calcium doped $MAPbI_3$with better energy state alignment in perovskite solar cells," *Applied Physics Letters*, vol. 112, no. 19, article 193901, 2018.

[51] M.-C. Wu, T.-H. Lin, S.-H. Chan, and W. F. Su, "Improved efficiency of perovskite photovoltaics based on Ca-doped methylammonium lead halide," *Journal of the Taiwan Institute of Chemical Engineers*, vol. 80, pp. 695–700, 2017.

[52] Q. Wang, Z. Jin, D. Chen et al., "μ-Graphene crosslinked $CsPbI_3$ Quantum dots for high efficiency solar cells with much improved stability," *Advanced Energy Materials*, vol. 8, no. 22, p. 1800007, 2018.

[53] B. Tang, L. J. Ruan, C. Qin, A. Shu, H. He, and Y. Ma, "High stability and temperature-dependent photoluminescence of orthorhombic $CsPbI_3$ Perovskite nanoparticles," *Advanced Optical Materials*, vol. 8, no. 16, article 2000498, 2020.

[54] G. Li, H. Wang, Z. Zhu et al., "Shape and phase evolution from $CsPbBr_3$ perovskite nanocubes to tetragonal $CsPb_2Br_5$ nanosheets with an indirect bandgap," *Chemical Communications*, vol. 52, no. 75, pp. 11296–11299, 2016.